Chinese Chemical Letters 32 (2021) 2994–3006

Contents lists available at ScienceDirect

Chinese Chemical Letters

journal homepage: www.elsevier.com/locate/cclet

Review

Recent progress in carbon-dots-based nanozymes for chemosensing and biomedical applications

Deming He, Minmin Yan, Pengjuan Sun, Yuanqiang Sun*, Lingbo Qu, Zhaohui Li*

College of Chemistry, Green Catalysis Center, Henan Joint International Research Laboratory of Green Construction of Functional Molecules and Their Bioanalytical Applications, Zhengzhou Key Laboratory of Functional Nanomaterial and Medical Theranostic, Zhengzhou University, Zhengzhou 450001, China

ARTICLE INFO

Article history:
Received 24 February 2021
Received in revised form 29 March 2021
Accepted 30 March 2021
Available online 31 March 2021

Keywords:
Carbon dots
Nanozyme
Chemosensing
Catalytic activity
Bioimaging

ABSTRACT

Nanozymes are nanomaterials with enzyme-like activities that efficiently overcome the drawbacks of natural enzymes in biosensing, detection, and biomedical fields, and they are the most widely used artificial enzymes. Owing to their excellent catalytic characteristics, biocompatibility, and environmental favorability, carbon-dots-based (CDs) nanozymes have inspired a research upsurge. However, no review focusing on CDs nanozymes has been published, even though substantial advances have been achieved. Herein, the advances, catalytic activities, and applications of CDs nanozymes are highlighted and summarized. In addition, the critical issues and challenges of researching nanozymes are discussed. We hope that this review will broaden the horizons of nanozymes and CDs nanozymes, as well as promote their development.

1. Introduction

Enzymes are involved as efficient biocatalysts in many physiological processes and reactions in multicellular organisms [1]. Nonetheless, natural enzymes have several drawbacks that severely hinder their development and application; they are unstable (easily denatured), expensive, and extremely sensitive to the external conditions, which affect their catalytic activities [2–4]. Thus, artificial enzymes, especially combined with nanotechnology, that can maintain excellent catalytic activities and overcome these drawbacks have attracted considerable interest. Since Pasquato *et al.* introduced triazacyclononane-functionalized gold nanoparticles (NPs) with phosphoesterase-like activity in 2004, and Yan *et al.* reported Fe_3O_4 NPs with inherent peroxidase-like characteristics in 2007, nanozymes containing diverse artificial nanomaterials that possess inherent enzyme-like characteristics have garnered considerable attention [5,6]. Compared with natural enzymes, nanozymes are favorable because they are low cost, produced in large scale, and possess remarkable catalytic activities. Hence, chemists have become very interested in nanozyme technology as an emerging artificial enzyme field to link nanotechnology and biomedical applications, rather than just being a concept [7].

As the most diverse emerging class of nanomaterials, carbon dots (CDs) have become widely known because of their remarkable biocompatibility, excellent photophysical characteristics, low cytotoxicity, inexpensive precursors, stability, and economic preparation [8–14]. Various CD-based nanocomposites, including carbon nanodots, carbon quantum dots, graphene quantum dots, and other element-doped CDs, have been developed and widely used in biosensing, photocatalysis, theranostics, and biomedical applications [15–23]. In addition, considerable research funding for CDs nanozyme investigations has been awarded in recent years owing to their intrinsic excellent catalytic characteristics. The environmental favorability of CDs nanozymes is the greatest advantage over semiconductor NPs and organometallic nanozymes which include heavy metals and are not suit for practical biomedical research [24].

Although a variety of remarkable and comprehensive reviews on nanozymes have been reported, no review focusing on CDs nanozymes has been published [25–30]. In this review, we summarize newly developed CDs nanozymes, as well as their corresponding catalytic characteristics and biomedical applications (Scheme 1). We hope that this review will aid in a better understanding of nanozymes and provide references for future design of CDs nanozymes, advancing the combination of the nanozyme and nanotechnology fields.

2. Classification of CDs nanozymes

Newly reported CDs-based redox nanozymes can be divided into four catalytic types: peroxidase, oxidase, catalase, and superoxide dismutase (SOD). According to the different substrates and products after the enzymatic reaction, these four types of

* Corresponding authors.
E-mail addresses: sunyq@zzu.edu.cn (Y. Sun), zhaohui.li@zzu.edu.cn (Z. Li).

https://doi.org/10.1016/j.cclet.2021.03.078

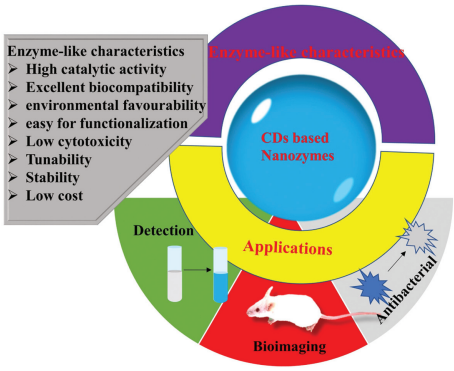

Scheme 1. Schematic illustration of CDs nanozymes and their corresponding enzyme-like activities and applications.

nanozymes are classified in Scheme 2 [4]. Some substrates that are widely used in nanozyme biosensors [28,29] are 3,3′,5,5′-tetramethylbenzidine (TMB), *o*-phenylenediamine (OPD), 2,2′-azino-bis(3-ethylbenzothizoline-6-sulfonic acid) (ABTS), and Amplex Red (AR) [30–32]. TMB, OPD, and ABTS are colorless, and they can be oxidized to blue (TMB_{ox}, λ_{abs} = 652 nm), yellow (phenazine-2,3-diamine (OPD_{ox}), λ_{abs} = 564 nm), and green ($ABTS_{ox}$, λ_{abs} = 420 nm) oxidation products by peroxidases, respectively. AR is colorless and nonfluorescent, and it can be oxidized to resorufin (red under room light and yellow emission at 585 nm), which can be further oxidized to resazurin (purple under room light and nonfluorescent).

2.1. CDs peroxidase

Peroxidases can catalyze oxidation of peroxides (H_2O_2 and some organic hydroperoxides), which are transformed into water. In 2014, Shamsipur *et al.* reported carbon quantum dots (**CDs-1**) that possess peroxidase activity to monitor the glutathione (GSH) level in human blood [31]. They used $Na_2EDTA{\cdot}2H_2O$ as the raw material, which was heated at 400 °C under argon for 2 h in a tube furnace to give **CDs-1** possessing peroxidase activity (Fig. 1). **CDs-1** can be used as the peroxidase to catalyze the reaction of TMB to TMB_{ox} with H_2O_2, accompanied by a color change from colorless to blue. There was almost no reaction between TMB I and II and H_2O_2 without **CDs-1**. Upon addition of **CDs-1**, three obvious emission peaks were observed at 370, 450 and 653 nm. They suggested that the electrons of the amino group of TMB were transferred to **CDs-1**, which increased the rate of electron transfer from **CDs-1** to H_2O_2, finally catalyzing the reaction of H_2O_2 with TMB. The absorption intensity at 653 nm was significantly weaker when GSH was added. The absorption intensity showed a good linear relationship with the GSH concentration in the range of 0–7 mmol/L, and the detection limit was 3 mmol/L. Moreover, the nonthiol compound showed little interference in detection of GSH because the sulfhydryl moiety possesses remarkable hydrogen-donating power. Because other biothiols, such as cysteine (Cys) and homocysteine (Hcy), existed in low concentrations in the organism, they could be ignored when the blood was diluted 1000 times, indicating that **CDs-1** can be used for specifically monitoring the GSH level in human blood.

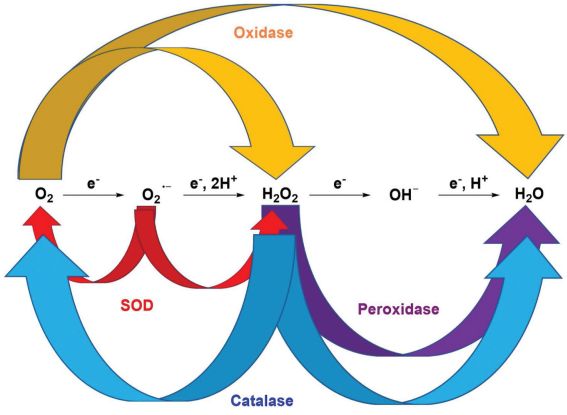

Scheme 2. Schematic diagram of different catalytic reactions using peroxidase, oxidase, SOD, and catalase. Reproduced with permission [4]. Copyright 2019, Royal Society of Chemistry.

Yousefinejad *et al.* developed novel **Fe-CDs-2** as a peroxidase mimic to detect H_2O_2 at the nanomolar level [32]. **Fe-CDs-2** was synthesized by integrating **CDs-2** and Fe_3O_4 NPs at a ratio of 4:1 under acidic conditions, and **CDs-2** was prepared using carbon soot and nitric acid as precursors (Fig. 2). Transmission electron microscopy images showed that **Fe-CDs-2** was a hemisphere with a size of about 10 nm. **Fe-CDs-2** was capable of catalyzing oxidation of TMB to TMB_{ox} with H_2O_2, accompanied by a color change from colorless to blue. TMB_{ox} exhibited higher absorbance with **Fe-CDs-2** than with **CDs-2** and Fe_3O_4 NPs alone under the same conditions. In the presence of TMB and **Fe-CDs-2**, the absorbance showed a remarkable linear relationship with the H_2O_2 concentration from 10 nmol/L to 1 mmol/L, accompanied by an extremely low detection limit of 1 nmol/L.

Guo *et al.* reported folic acid (**FA**)**-CDs-3** with peroxidase activity for detection and treatment of cancer cells [33]. **FA-CDs-3** was synthesized by combining $Fe_3(PO_4)_2{\cdot}8H_2O$ with **CDs-3**, which were synthesized using ammonium citrate and FA-NH_2 as raw materials (Fig. 3). Because of overexpression of FA receptors on the surface of tumor cell membranes, FA is a remarkable targeting ligand that can target various tumor cells. **FA-CDs-3** is capable of catalyzing oxidation of TMB by H_2O_2, indicating its peroxidase activity. When HeLa cells and normal HEK293 T cells were incubated with **FA-CDs-3** for 2 h, washed with phosphate-buffered saline (PBS) to remove the unattached **FA-CDs-3**, and then treated with TMB and H_2O_2, a blue color change occurred in the solution with HeLa cells, while there was little change in the solution with HEK293 T cells, indicating that **FA-CDs-3** can target HeLa cells. Moreover, **FA-CDs-3** catalyzed exogenous H_2O_2 to produce $^{\bullet}OH$, which disrupted the redox balance in the cancer cells and induced apoptosis of the cancer cells. Although ascorbic acid (AA) is commonly used to induce apoptosis, a large dose of AA is needed to induce cells to produce H_2O_2 and generate numerous reactive oxygen species (ROS) through oxidative stress to induce cell death. When HeLa cells were co-incubated with 0.5 mmol/L AA and 50 μg/mL **FA-CDs-3** for 48 h, 67% of the HeLa cells showed apoptosis. By contrast, normal HEK293 T cells incubated with high doses of **FA-CDs-3** and AA exhibited only 20% cytotoxicity, suggesting that **FA-CDs-3** has the potential to specifically detect and treat cancer cells.

Shi *et al.* developed two types of surface-functionalized CDs (**CDs-4.1** and **CDs-4.2**) with peroxidase activity to explore how the surface structure influences the catalytic performance of CDs [34]. **CDs-4** was synthesized by the hydrothermal method using citric acid and thiourea as raw materials (Fig. 4). Different surface modifications were then performed to obtain positively charged poly(ethyleneimine)-modified CDs (**CDs-4.1**) and negatively charged citric acid-modified CDs (**CDs-4.2**). **CDs-4**, **CDs-4.1**, and **CDs-4.2** catalyzed oxidation of TMB and ABTS to their corresponding oxidation products using H_2O_2. The activity of **CDs-4.1** in catalyzing ABTS and the activity of **CDs-4.2** in catalyzing TMB were higher than those of **CDs-4**, indicating that **CDs-4.1** and **CDs-4.2** showed excellent peroxidase-like activity. Moreover, when catalytic oxidation of TMB was performed, the absorbance value of

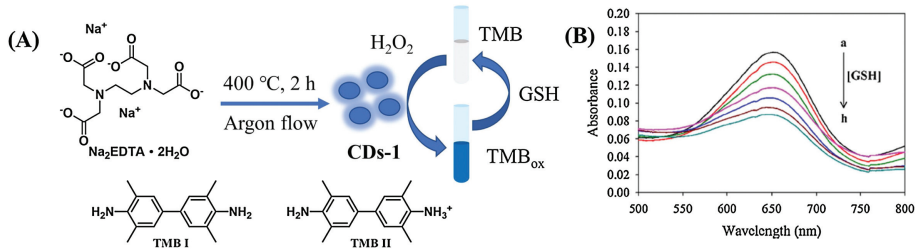

Fig. 1. (A) Synthesis process and proposed mechanism of **CDs-1** reacting with TMB I and II in the presence of H_2O_2, respectively, and then reacting with GSH. (B) Absorbance of TMB_{ox} with increasing GSH. Copied with permission [31]. Copyright 2014, Elsevier.

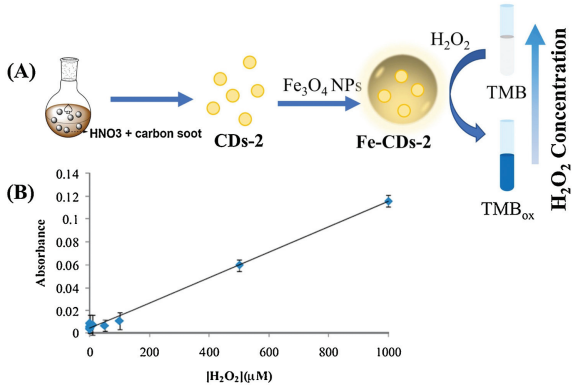

Fig. 2. (A) Synthesis route of **Fe-CDs-2** and **Fe-CDs-2** catalysis of TMB oxidation by H_2O_2. (B) Absorbance of TMB_{ox} at 653 nm with the increasing H_2O_2 concentration (μM: μmol/L). Copied with permission [32]. Copyright 2017, Elsevier.

CDs-4.2 at 652 nm was higher than that of **CDs-4**, and the absorbance of **CDs-4.1** was the weakest. This might be because of the relatively strong affinity between the two amino groups of TMB and the negatively charged surface of **CDs-4.2**, whereas the affinity between the positively charged surface of **CDs-4.1** and TMB is relatively weak. For ABTS containing two sulfonic groups, the catalytic activity of **CDs-4.2** for ABTS was less than that for TMB, while the catalytic activity was the opposite for **CDs-4.1**. In addition, surface-functionalized **CDs-4.1** and **CDs-4.2** did not change the catalytic mechanism, which was that the CDs catalyzed H_2O_2 to produce $^{\bullet}OH$, while surface modification enhanced electron transfer.

Zhao *et al.* reported novel **CDs-5** with excellent peroxidase activity to detect the cholesterol content in human serum [35]. **CDs-5** was prepared by a one-step solvothermal method using MoS_2 and ethanol as raw materials (Fig. 5). Co-doping of Mo and S improved the yield and peroxidase activity of the CDs. In the presence of H_2O_2, **CDs-5** catalyzed oxidation of TMB to TMB_{ox}, which showed two characteristic absorption peaks at 369 and 652 nm. Interestingly, cholesterol enzymes catalyzed cholesterol and generated H_2O_2, which promoted oxidation of TMB without exogenous H_2O_2. The absorbance at 652 nm showed a good linear relationship with the cholesterol concentration in the range 0.01–0.6 mmol/L, and the detection limit was 7 μmol/L. **CDs-5** showed high stability and almost no change in the catalytic activity after 20 days, and it was successfully applied to detect the cholesterol content in human serum.

Chen *et al.* reported **CDs-6** with peroxidase activity to selectively detect the pyrophosphate ion (PPi) concentration in human urine [36]. They used galactose and histidine, which were refluxed in NaOH to give **CDs-6** (Fig. 6). **CDs-6** catalyzed oxidation of TMB, OPD, and AR in the presence of H_2O_2, which was confirmed by the appearance of the corresponding absorption peaks at 652, 450, and 585 nm, respectively. When the above system was treated with the PPi, the absorption peak disappeared. When horseradish peroxidase (HRP) was used to catalyze oxidation of TMB and AR, the absorbance showed a negligible change after addition of the PPi. These phenomena can be attributed to the interaction between the amino and carboxyl groups on the surface of **CDs-6** and the PPi, resulting in inhibition of electron transfer and interruption of the catalytic reaction. Thus, **CDs-6** can detect the PPi, and the detection limit was calculated to be 4.29 nmol/L. Furthermore, a portable kit was prepared by setting **CDs-6** and OPD on paper. The color of the

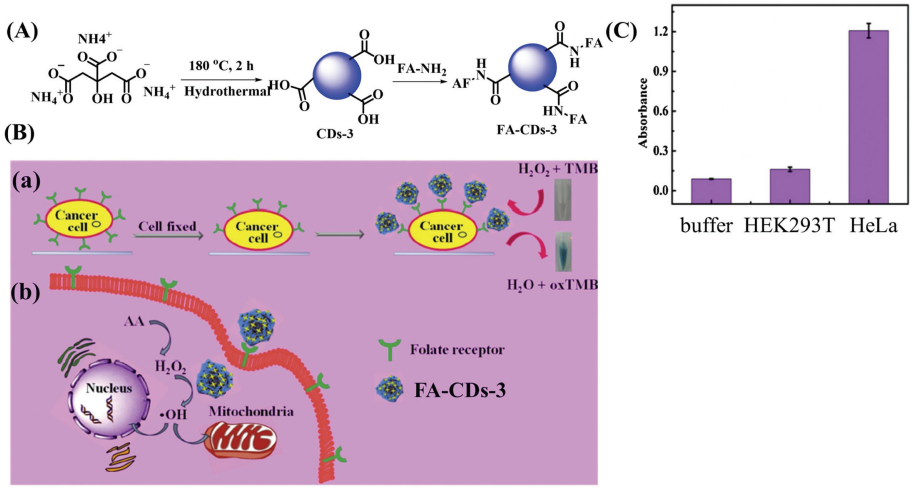

Fig. 3. (A) Synthesis route of **FA-CDs-3**. (B) Schematic diagram of **FA-CDs-3** for (a) detecting and (b) treating cancer cells. (C) Absorbance of different solutions (buffer, HEK293 T, and HeLa cells) at 652 nm. Reproduced with permission [33]. Copyright 2019, Elsevier.

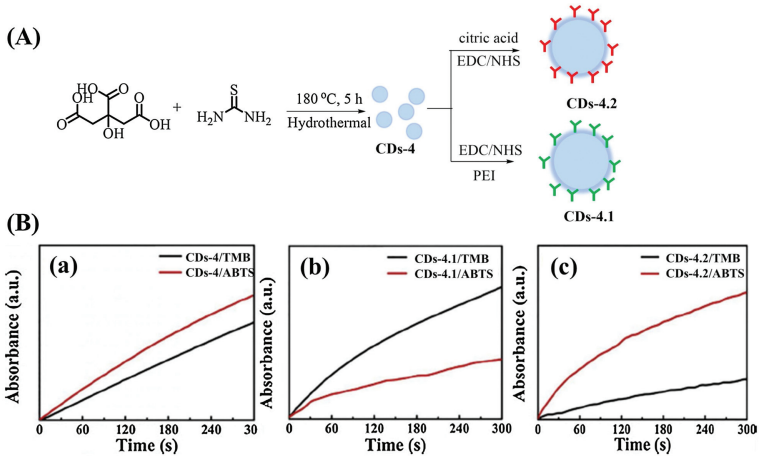

Fig. 4. (A) Synthesis routes of **CDs-4**, **CDs-4.1** and **CDs-4.2**. (B) Absorbance of TMB_{ox} (652 nm) and $ABTS_{ox}$ (416 nm) under different CDs: (a) **CDs-4**, (b) **CDs-4.1** and (c) **CDs-4.2**. Reproduced with permission [34]. Copyright 2019, Elsevier.

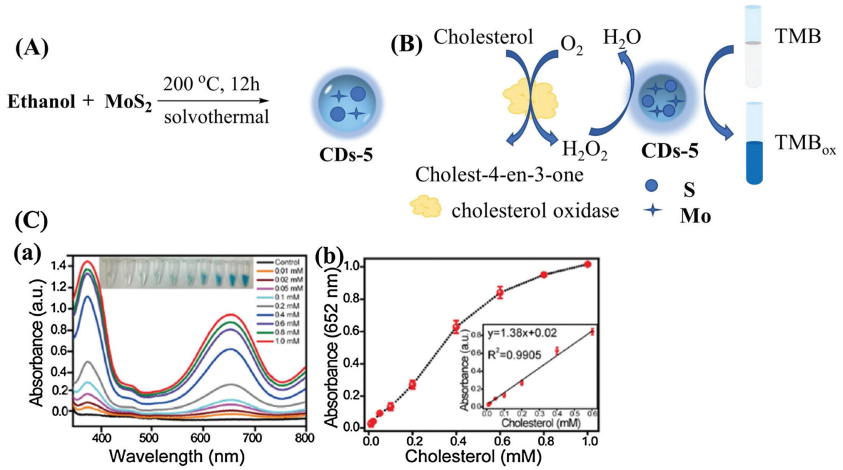

Fig. 5. (A) Synthesis route of **CDs-5**. (B) Mechanism of cholesterol detection by applying cholesterol and **CDs-5**. (C) (a) Absorbance of TMB for cholesterol detection and (b) calibration curves of (a) (mM: mmol/L). Copied with permission [35]. Copyright 2019, Royal Society of Chemistry.

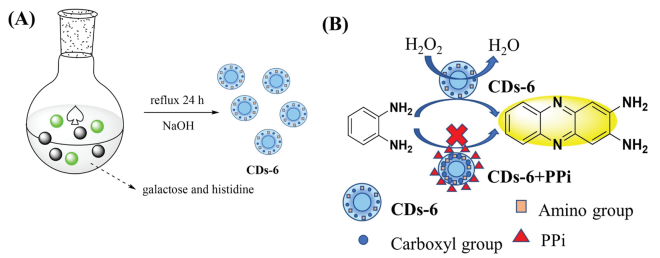

Fig. 6. (A) Synthesis of **CDs-6**. (B) The sensing mechanism of PPi by its inhibition effect toward the peroxidase activity of **CDs-6**.

paper turned pale with increasing PPi concentration, and the detection limit was about 39.2 nmol/L, which is 500 times lower than the PPi concentration in healthy human urine [37–39].

Li *et al.* reported copper-doped CDs (**CDs-7**) as a peroxidase mimic to detect chromium ions [Cr(III)] [40]. **CDs-7** was synthesized from Na_2[Cu(EDTA)], which was heated at 270 °C in a tube furnace for 2 h under N_2 (Fig. 7). In the presence of **CDs-7**, OPD was oxidized in DAP by H_2O_2, which emitted yellow fluorescence at 564 nm under excitation of 421 nm. When Cr(III) was added, a new absorption peak at 400 nm appeared and the fluorescence intensity of the generated DAP immediately decreased. The new absorption peak showed good overlap with excitation of DAP, which was absorbed by Cr(III), resulting in fluorescence quenching through the well-known inner filter effect (IFE) mechanism [41–43]. The fluorescence intensity of DAP showed a remarkable linear relationship with the Cr(III)

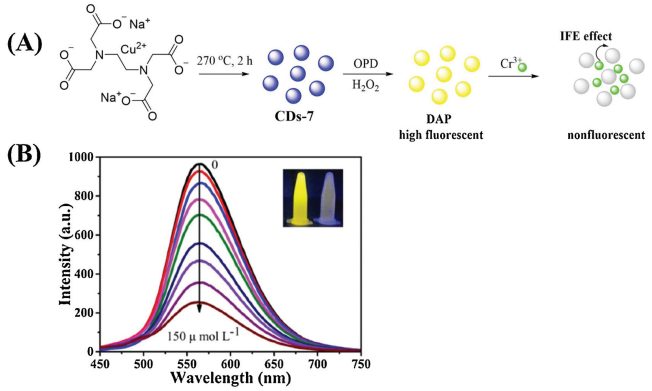

Fig. 7. (A) Synthesis and detection mechanism of **CDs-7** with peroxidase activity for Cr(III). (B) Fluorescence intensity of DAP with increasing Cr(III) concentration. Copied with permission [40]. Copyright 2020, Elsevier.

concentration in the range 5–150 μmol/L, accompanied by an extremely low detection limit of 0.12 μmol/L. Finally, because Cr (VI) can be reduced to Cr(III) by using ABTS, **CDs-7** was successfully used to directly detect Cr(III) and total Cr in water samples. The concentration of Cr(VI) can then be indirectly calculated, which provides a novel and effective approach for environmental detection of Cr(III) and Cr(VI).

Wang *et al.* reported new iodine-containing CDs (**CDs-8**) with peroxidase-like and antibacterial activities through activating H_2O_2 under room light [44]. **CDs-8** was prepared by heating iohexol at 180 °C for 8 h in an autoclave (Fig. 8). **CDs-8** catalyzed oxidation of TMB to TMB_{ox} by H_2O_2, accompanied by appearance of a new absorption peak at 652 nm and a color change from colorless to blue. There was little antibacterial activity when **CDs-8** or H_2O_2 alone was added to *Staphylococcus aureus* and *Escherichia coli*. However, when **CDs-8** and H_2O_2 were added together, the bacterial shape changed from rod-shaped to wrinkled, and the cell membrane integrity was destroyed by the generated hydroxyl radicals ($^{\bullet}OH$), resulting in bacterial death. Furthermore, the antibacterial activity was significantly influenced by the ratio of **CDs-8** to H_2O_2 and whether they were exposed to room light. In addition, **CDs-8** successfully accelerated wound healing even though the exogenous H_2O_2 concentration was extremely low (0.07 mmol/L), indicating that **CDs-8** can be used as an antibacterial agent and for wound healing.

Ibarbia *et al.* reported a graphene oxide quantum dot (**CDs-9**) based hydrogel functionalized by the cross-linkable 3-(triethoxysilyl)propyl methacrylate (MPS) group (**CDs-9-MPS-A50coS50**) to photodegrade rhodamine B (RhB) [45]. **CDs-9** was prepared by refluxing a mixture of XC-72 carbon black and HNO_3 aqueous solution for 72 h (Fig. 9). A mixture of **CDs-9** and MPS, as a cross-linker, was stirred in ultrapure water for 24 h to obtain **CDs-9-MPS**. **CDs-9-MPS** showed high peroxidase ability with 45% decomposition of RhB in the dark and 92% decomposition of RhB in room light. When H_2O_2 and **CDs-9-MPS** were added, the absorbance of RhB at 554 nm was quenched, along with a color change from pink to pale orange. The degradation mechanism is that the $^{\bullet}OH$ radicals generated from H_2O_2 in the process of photodegradation show high oxidation activity for RhB. Furthermore, **CDs-9-MPS** was incorporated into the poly[2-(methacryloyloxy)ethyl]trimethylammonium]-*co*-(3-sulfopropylmethacrylate) 50:50 (**A50coS50**) hydrogel to obtain the **CDs-9-MPS-A50coS50** hydrogel. The **CDs-9-MPS-A50coS50** hydrogel showed a similar trend for degradation of RhB in the dark to the hydrogel-free sample. The 2.5% **CDs-9-MPS-A50coS50** hydrogel showed 10% degradation for RhB after 6 h, which was slightly higher than that of the hydrogel-free sample (4%). When irradiated by visible light, decomposition of RhB by the 2.5% **CDs-9-MPS-A50coS50** hydrogel increased from 20% to 50%, while that of the hydrogel-free sample was only enhanced from 4% to 20%, indicating the remarkable photocatalytic activity of the 2.5% **CDs-9-MPS-A50coS50** hydrogel. In addition, all of the RhB was completely degraded by the 2.5% **CDs-9-MPS-A50coS50** hydrogel after 24 h, and the hydrogel showed excellent long-term stability in water, which means that the **CDs-9-MPS-A50coS50** hydrogel is a promise material for degradation of organic dyes in aqueous solution.

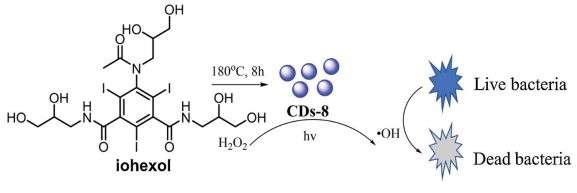

Fig. 8. Mechanism of **CDs-8** with antibacterial activity in the presence of H_2O_2.

Li *et al.* reported CDs (**CDs-10-Cu_4O_3**) that stabilized Cu_4O_3 as nanozymes with high stability and catalytic activities (dual oxidase- and peroxidase-like activities) [46]. **CDs-10-Cu_4O_3** was obtained by hydrothermal reaction using **CDs-10** and CuCl as raw materials, and **Cu_4O_3** was prepared by the same approach using CuCl as the raw material (Fig. 10). **CDs-10-Cu_4O_3** catalyzed oxidation of OPD to OPD_{ox} and showed higher catalytic activity than **Cu_4O_3** both in the dark and under light. The V_{max} value of **CDs-10-Cu_4O_3** was 20.93 μmol L^{-1} min^{-1} in the dark, which was 2.55-times higher than that of Cu_4O_3 (8.22 μmol L^{-1} min^{-1}) from the kinetic parameters. Furthermore, **CDs-10-Cu_4O_3** also catalyzed oxidation of dopamine (DA) to oxidative dopamine (DA_{ox}). The V_{max} values of **CDs-10-Cu_4O_3** were 4.21 and 6.67 μmol L^{-1} min^{-1} under dark and light conditions, which were higher than those of Cu_4O_3 (2.02 and 3.85 μmol L^{-1} min^{-1}). The above results indicated that **CDs-10-Cu_4O_3** possesses excellent enzyme activity because of its rich Cu^{2+}/Cu^{+} redox couples. The reaction mechanism is that **CDs-10-Cu_4O_3** reduces absorbed O_2 to $^{\bullet}O_2^-$ or H_2O_2, along with oxidation of Cu^{+} to Cu^{2+}. Owing to coordination of Cu^{2+} to the amino units of **CDs-10**, Cu^{2+} can accept the delocalized electrons from **CDs-10** to revert to Cu^{+}. The catalytic activities were significantly affected by the pH, temperature, and other oxidizing agents.

Li *et al.* reported a type of Fe_3C/N-doped nanozyme (**CDs-11**) to efficiently heal wounds by suppressing bacterial infection [47]. **CDs-11** was prepared through an electrochemical strategy using $FeSO_4{\cdot}H_2O$ and histidine (His) as the electrolyte (Fig. 11). The anode and cathode were a graphite rod and a Pt sheet, respectively, and the electrolysis reaction was completed by stirring for 8 h to obtain grey-black **CDs-11**. In the presence of **CDs-11**, H_2O_2 produced $^{\bullet}OH$, oxidizing colorless TMB to a blue product (TMB_{ox}) *in vitro*. **CDs-11** exhibited the best peroxidase-like activity at 50 °C in the temperature range of 25–70 °C, and at pH 4.0 in the pH range of 1.0–12.0. The V_{max} value from the Lineweaver–Burk equation was higher than those of other nanozymes, suggesting its outstanding catalytic activity. In further studies, *E. coli* and *S. aureus* were treated with PBS, H_2O_2, **CDs-11** and **CDs-11** + H_2O_2. When incubated with **CDs-11** + H_2O_2, bacterial colonies were hardly observed compared with other control groups. Scanning electron microscopy (SEM) confirmed that the cell morphology was rough and damaged when treated with only **CDs-11** + H_2O_2. The *E. coli* cells treated with **CDs-11** + H_2O_2 were observed to be damaged by a confocal microscope. Furthermore, when Sprague-Dawley rats with a bacterial infection by *S. aureus* were treated with **CDs-11** + H_2O_2, the wounds gradually healed after 6 days and fewer bacterial colonies were detected compared with other groups treated with PBS, H_2O_2, and **CDs-11**. The above results showed that **CDs-11** can accelerate wound healing because it catalyzes oxidation of hydrogen peroxide to $^{\bullet}OH$.

Liang *et al.* reported enzyme-like **CDs-12** that inhibits bacterial infections through destroying the biofilms of the bacteria [48]. First, citric acid and formamide were added to an autoclave and heated at 180 °C for about 12 h to obtain the CD precursor, and then **CDs-12** was obtained by integrating the CDs with Pt NPs (Fig. 12). **CDs-12** efficiently catalyzed H_2O_2 oxidation of TMB, OPD, and ABTS to TMB_{ox}, OPD_{ox} and $ABTS_{ox}$, respectively. Owing to its excellent properties, **CDs-12** can also be used as a potent disinfection nanoagent. When spherical-like *S. aureus* (MRSA) and rod-shaped *E. coli* were treated with **CDs-12** in the presence of H_2O_2, SEM showed that the bacterial membrane became rough and was damaged. The mechanism is that the $^{\bullet}OH$ generated from H_2O_2 destroys the bacterial colonies by cleavage of the proteins and nucleic acids, causing bacterial death. The antibacterial effect was more obvious for higher concentration of hydrogen peroxide. In further studies, when MRSA-infected mice were treated with **CDs-12**, the wounds showed excellent healing after 7 days

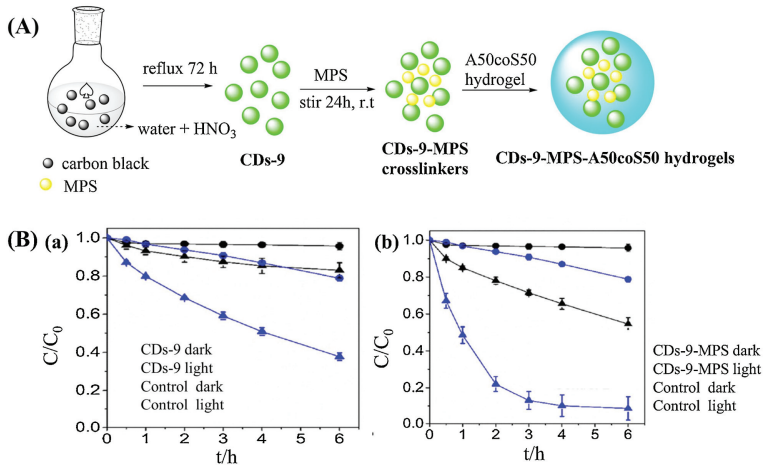

Fig. 9. (A) Synthesis of **CDs-9-MPS-A50coS50**. (B) Degradation of RhB by H_2O_2 using (a) **CDs-9** and (b) **CDs-9-MPS** in the dark and under room light. Reproduced with permission [45]. Copyright 2020, Elsevier.

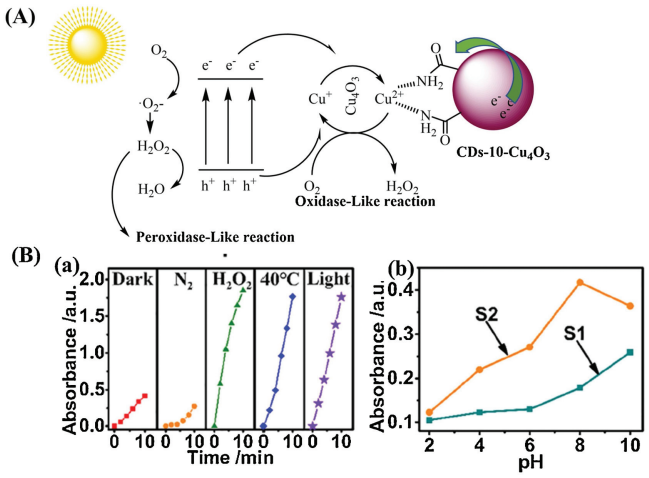

Fig. 10. (A) Catalytic reaction mechanism of **CDs-10-Cu_4O_3**. (B) (a) Enzyme-like activities of **CDs-10-Cu_4O_3** under different influencing factors at the same pH and (b) enzyme-like activities of **CDs-10-Cu_4O_3** at different pH values. Copied with permission [46]. Copyright 2020, Elsevier.

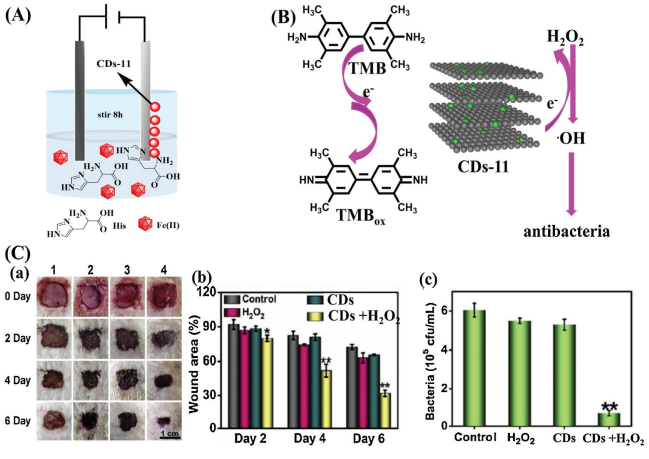

Fig. 11. (A) Synthesis of **CDs-11**. (B) Oxidation and antibacterial mechanisms of **CDs-11** (TMB as the substrate). (C) (a) Wound changes of rats treated with PBS, H_2O_2, **CDs-11**, and **CDs-11** + H_2O_2, (b) changes of the wound area, and (c) number of different bacterial colonies. Reproduced with permission [47]. Copyright 2020, Elsevier.

compared with the control group. Note that from the inflammation triggered around the wound, the produced endogenous H_2O_2 participated in the reaction without additional H_2O_2.

Su *et al.* reported CDs (**Hemin-CDs-13**) with peroxidase-like activity for colorimetric and fluorometric sensing of hydrogen peroxide, glucose, and xanthine [49]. **CDs-13** was prepared using citric acid and urea, which were dissolved in dimethylformamide and transferred into an autoclave at 160 °C for 6 h (Fig. 13). The synthesized **CDs-13** emitted a strong fluorescence signal at 540 nm under excitation of 480 nm. The obtained **CDs-13** was then self-assembled with hemin by stirring for 7 h at room temperature to form **Hemin-CDs-13**. The peroxidase-like activity of **CDs-13**, hemin, and **Hemin-CDs-13** was compared. Hemin showed much less activity owing to it poor water solubility and **CDs-13** showed no catalytic activity. Thus, introduction of **CDs-13** efficiently increased dispersion. The generated **Hemin-CDs-13** exhibited high peroxidase-like activity, and 4-aminoantipyrine (4-AAP) and phenol were oxidized to the red quinoneimine dye by H_2O_2, accompanied by fluorescence quenching of **Hemin-CDs-13**. In further H_2O_2-detection studies, the absorbance of the quinoneimine dye at 505 nm was enhanced and the fluorescence intensity of **Hemin-CDs-13** at 540 nm decreased with increasing concentration of H_2O_2 in the range 0.17–333 μmol/L. In addition, the solution color gradually darkened from light red. The detection limits of the fluorescent and colorimetric assays were 0.15 and 0.11 μmol/L, respectively. In the presence of glucose or xanthine, similar experimental phenomena to H_2O_2 were observed. This was attributed to glucose and xanthine being able to generate H_2O_2 under oxidation of glucose oxidase (GOx) and xanthine oxidase (XOD). In general, **Hemin-CDs-13** can be applied to detect the species related to the H_2O_2-generation reaction.

Yang *et al.* reported **CDs-14** nanozymes with dual oxidase- and peroxidase-like activities in a neutral environment [50]. **CDs-14** was prepared from Na_2[Cu(EDTA)] and AA, which were heated at 270 °C for 2 h in a quartz glass tube to give **CDs-14** with yellow fluorescence (Fig. 14). The as-prepared **CDs-14** catalyzed oxidation of OPD to OPD_{ox} by H_2O_2 and O_2. The oxidation mechanism is that Cu^+ from **CDs-14** reduces H_2O_2 and O_2 to generate $^{\bullet}OH$ and $^{\bullet}O_2^-$, respectively, which further oxidize OPD to OPD_{ox}. With the assistance of ferrous ions, the catalytic activity of **CDs-14** exhibited excellent enhancement owing to generation of $^{\bullet}OH$ and $^{\bullet}O_2^-$, which were decomposed by H_2O_2 under the reaction of ferrous ions. The lower K_m value and higher V_{max} value suggested that the ferrous ions play a crucial role in the catalytic process. Notably, the fluorescence of **CDs-14** + Fe^{2+}/H_2O_2 was only quenched in the

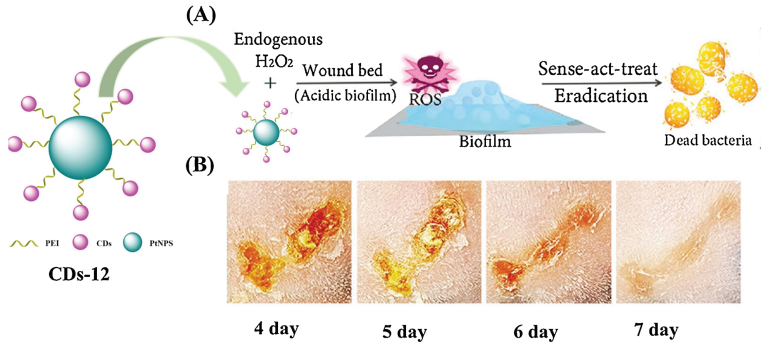

Fig. 12. (A) Process of biofilm eradication mediated by **CDs-12**. (B) Changes of the wound infected by MRSA treated with **CDs-12** during 7 days. Copied with permission [48]. Copyright 2020, Wiley Publishing Group.

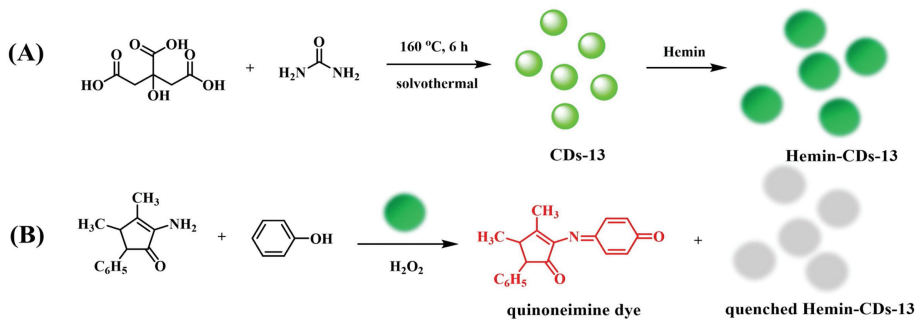

Fig. 13. (A) Synthesis route of **CDs-13** and **Hemin-CDs-13**. (B) Mechanism of oxidation of 4-AAP and phenol by H_2O_2 catalyzed by **Hemin-CDs-13**.

presence of Cr(III) ions. Further studies showed that the Cr(III) ions were transformed to CrO_2^-, which was further oxidized to CrO_4^{2-} by H_2O_2. The detection limit for Cr(III) was 36 nmol/L. The excellent selectivity and sensitivity of **CDs-14**/H_2O_2 indicate that it can be applied to detect Cr(III) in real water samples.

Li *et al.* reported a nanozyme (**CDs-15**) that can release DNAzyme to enhance its catalytic efficiency in the presence of K^+ [51]. **CDs-15** was prepared from corn starch and ethylenediamine (EDA) by the microwave method at 140 °C for 10 min (Fig. 15). When **CDs-15** was linked with an aptamer (Apt), **Apt-CDs-15** quenched the fluorescence of **CDs-15**, which was attributed to inhibition of the catalytic activity. **Apt-CDs-15** generated DNAzyme with hemin (HM) to improve the catalytic activity of **CDs-15** in the presence of K^+. **CDs-15** and DNAzyme co-catalyzed generation of TMB_{ox} with a fluorescence signal at 403 nm and an absorption band at 563 nm in the presence of H_2O_2. The fluorescence intensity of TMB_{ox} gradually increased with increasing concentration of **Apt-CDs-15** with K^+. Moreover, the low K_m value and high V_{max} value suggested that **Apt-CDs-15** possesses excellent affinity and high catalytic activity. The catalytic mechanism can be attributed to the rich π electrons on the **CDs-15** surface. The rich electrons promote electron transfer in the redox process of TMB and H_2O_2. The DNAzyme produced from **Apt-CDs-15** with K^+ can synergistically catalyze oxidation of TMB owing to the π-π electrons and accelerated redox reaction between TMB and H_2O_2. **CDs-15** was also used to detect ultra-trace K^+, and the detection limit was 0.024 nmol/L.

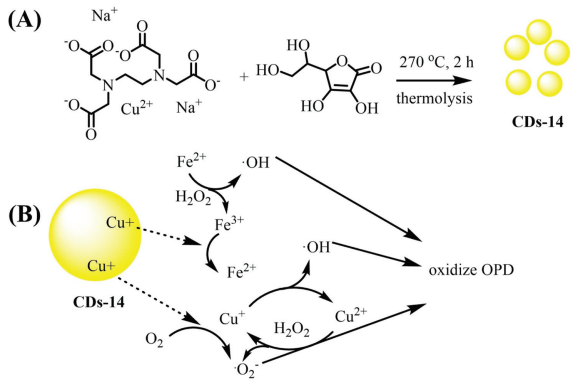

Fig. 14. (A) Synthesis process of **CDs-14**. (B) Mechanism of oxidation of OPD by **CDs-14** with the aid of Fe^{2+}.

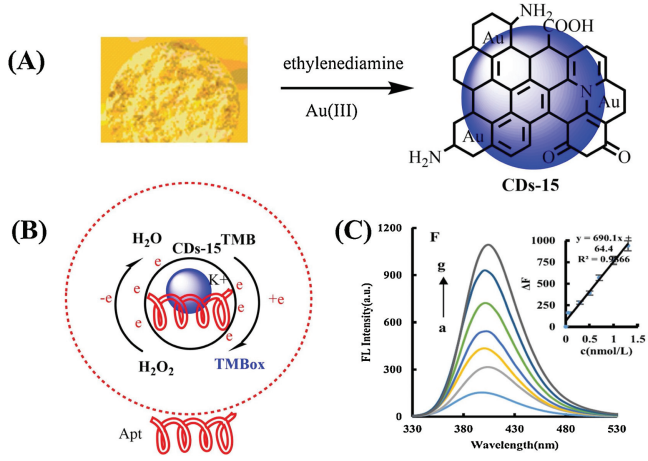

Fig. 15. (A) Synthesis process of **CDs-15**. (B) Oxidation mechanism of TMB in the presence of **Apt-CDs-15** and K^+. (C) Fluorescence intensity of TMB_{ox} with increasing K^+ concentration. Reproduced with permission [51]. Copyright 2020, Elsevier.

2.2. CDs oxidase

Oxidase plays a catalytic role in the oxidation process in the presence of oxygen, which is finally turned into H_2O_2, H_2O, or $^{\bullet}O_2^-$. Li *et al.* reported **Cu_2O-CDs-16** with light-boosting enzyme-like activity and high reaction rate [52]. **CDs-16** was prepared by mixing a solution containing coal pitch powder, formic acid, and H_2O_2, which were further reacted with copper(II) acetylacetonate ($Cu(acac)_2$) to give **Cu_2O-CDs-16** (Fig. 16). OPD was oxidized to OPD_{ox} in the presence of **Cu_2O-CDs-16** under light irradiation. Under visible light, the photogenerated holes and electrons participated in oxidation of OPD. The electrons on the surface reacted with O_2 to generate $^{\bullet}O_2^-$ radicals, and then combined with H^+ to form $^{\bullet}OH$. The photogenerated holes promoted generation of electrons to activate the N—H bond in OPD through accelerating the process of the self-oxidation reaction of Cu_2O. The kinetic parameter (K_m) of **Cu_2O-CDs-16** for OPD was 3.94 mmol/L, which is lower than those of reported mimic peroxidases, such as Cu@Cu_2O aerogels and $ZnFe_2O_4$ (K_m = 8.88 and 22.6 mmol/L, respectively) [53,54], suggesting that **Cu_2O-CDs-16** possessed better binding affinity to OPD. The V_{max} (9.47 μmol L^{-1} min^{-1}) was higher than that of the above nanocomposites and Cu_2O, indicating that **Cu_2O-CDs-16** possessed higher catalytic activity for OPD. Furthermore, **Cu_2O-CDs-16** with additional **CDs-16** showed higher activity for OPD than Cu_2O, which was attributed to **CDs-16** facilitating photogenerated carrier transfer.

Zhang *et al.* developed phosphorescent CDs (**CDs-17**) with oxidase activity for conversion of triplet oxygen ($^3O_2$) to singlet oxygen ($^1O_2$) [55]. **CDs-17** was prepared by hydrothermal polymerization using citric acid and EDA as raw materials (Fig. 17). TMB was oxidized by **CDs-17** in several seconds under 365 nm because **CDs-17** can catalyze formation of singlet oxygen, which can oxidize TMB. The phosphorescence intensity of **CDs-17** was related to the singlet oxygen emission and photosensitizing activity. Interestingly, the phosphorescence intensity increased with increasing reaction temperature because the CDs synthesized at higher temperature possessed higher nitrogen content. *E. coli* and *Salmonella* were incubated with **CDs-17** and phloxine B (PB, a photosensitizer) under dark and light conditions. For **CDs-17** in light, the two types of bacteria showed apparent growth inhibition, and the corresponding inhibition efficiency was nearly twice that of PB, indicating that **CDs-17** possesses remarkable antibacterial activity and can be used in photodynamic antibacterial chemotherapy.

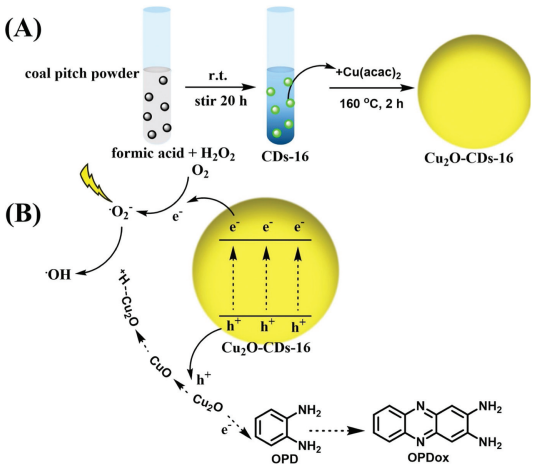

Fig. 16. (A) Synthesis route of **Cu_2O-CDs-16**. (B) Oxidation mechanism of TMB in the presence of **Cu_2O-CDs-16**.

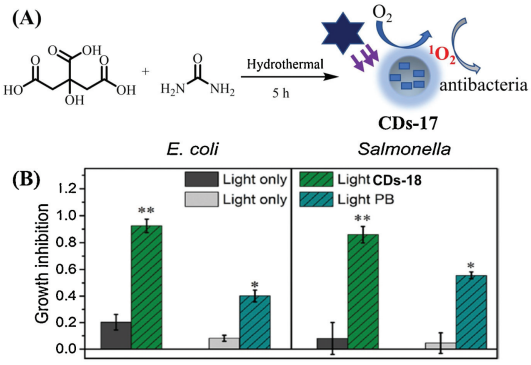

Fig. 17. (A) Synthesis route and photosensitization mechanism of **CDs-17** for bacteria. (B) Bacterial inhibition by **CDs-17** and PB under dark and light conditions. Reproduced with permission [55]. Copyright 2015, American Chemical Society.

Ren *et al.* reported novel CDs doped with copper (**CDs-18**) as an oxidase mimic for monitoring the level of hydroquinone (HQ) [56]. **CDs-18** was synthesized by the hydrothermal method using Cu $(NO_3)_2$ and poly(methacrylic acid) sodium salt as raw materials (Fig. 18). **CDs-18** emitted blue fluorescence at 460 nm and exhibited remarkable photostability and stability in a wide pH range (3.0–13.5). *p*-Phenylenediamine (PPD) is colorless, and it changed to brown in 30 min with addition of **CDs-18**, which catalyzed oxidation of PPD and generated a clear absorption peak at 495 nm. **CDs-18** also showed better temperature stability than laccase, and the optimum pH was 8.5. When polyacrylamide (PAM^+) was added to **CDs-18**, PPD and the oxidation product of PPD on the surface of **CDs-18** could be removed by flocculation between PAM^+ and **CDs-18**. In addition, **CDs-18** reacted with HQ with a color change from colorless to yellow in 10 min. In carbonate buffer (pH 9.2), the fluorescence intensity at 460 nm decreased with increasing HQ concentration, and the relative fluorescence quenching (I/I_0) showed a remarkable linear relationship with the HQ concentration in the range 0.05–2 mmol/L. The detection limit was 1 μmol/L, which is much lower than the maximum level specified by the Environmental Protection Agency of 3 μmol/L.

Zhang *et al.* developed Mn(II)-containing CDs (**CDs-19**) as a photo-oxidation nanozyme to improve the catalytic effect of CDs under physiological conditions (pH 7.4) and resolve the pH limitations [57]. Under irradiation of 365 nm light, the TMB solution was colorless, and upon addition of **CDs-19**, the solution was only blue at pH < 5. When Mn(II) was added to the above system, the solution was blue even at physiological pH (Fig. 19). The mechanism is that singlet oxygen is generated from **CDs-19** under light-oxidized Mn(II), and the oxidation product Mn(III) as a mediator further oxidizes TMB. Among common divalent metals, only Mn(II) was able to catalyze oxidation of TMB. Because Mn(III)/EDTA has high stability, when **CDs-19** was treated with EDTA, TMB was oxidized within 10 s. Furthermore, the amount of Mn(II) in the CDs was positively correlated with the absorbance of TMB at 652 nm, and the detection limit of Mn(II) was 5 nmol/L. Based on this strategy, many nanozymes could be explored for use in biosensing and nanotechnology at neutral pH.

Honarasa *et al.* developed **CDs-20** with oxidase activity for detection of trace Fe^{2+} [58]. **CDs-20** was synthesized by mixing $KMnO_4$ and CDs, which were prepared from candle dust using nitric acid (Fig. 20). **CDs-20** catalyzed oxidation of TMB to TMB_{ox} by oxygen, leading to appearance of the characteristic absorption peak at 655 nm. In addition, with increasing oxygen concentration, the blue color of the solution deepened. The increase of the absorbance at 655 nm proved that oxygen, as an oxidant, participated in oxidation of TMB and was reduced to H_2O. Notably, when Fe^{2+} was added to the solution, the absorbance at 655 nm

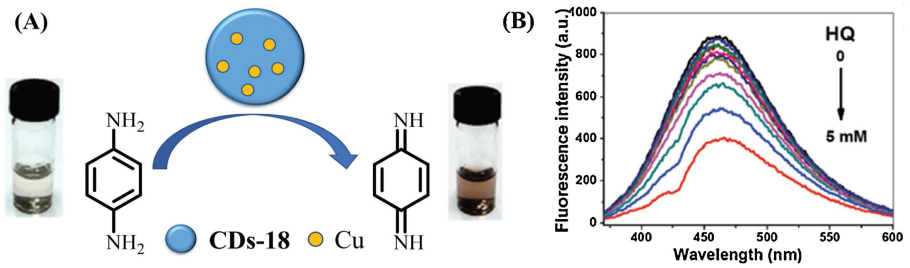

Fig. 18. (A) Schematic illustration of **CDs-18** reacting with PPD. (B) Fluorescence intensity change of **CDs-18** with increasing HQ concentration (mM: mmol/L) in carbonate buffer. Copied with permission [56]. Copyright 2018, Royal Society of Chemistry.

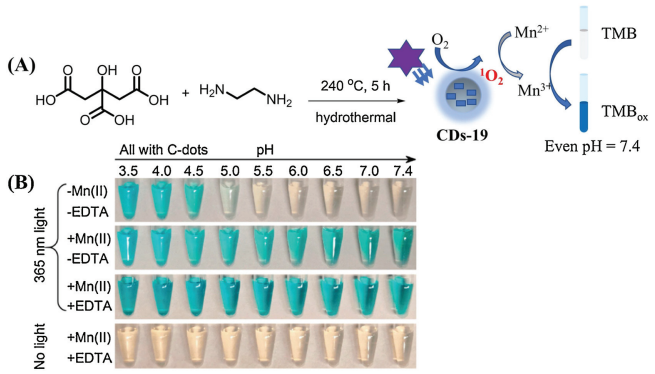

Fig. 19. (A) Synthesis route of **CDs-19** and mechanism of Mn(II) oxidation, which can increase the photo-oxidation characteristic of **CDs-19** under physiological conditions (pH 7.4). (B) Images of TMB oxidized by **CDs-19** with and without Mn(II) and EDTA under 365 nm light and different pH conditions. Copied with permission [57]. Copyright 2019, American Chemical Society.

decreased and the color became weaker, which was attributed to competitive oxidation of Fe^{2+} and TMB. Moreover, addition of other metal ions, such as Co^{2+}, Ni^{2+}, and Mn^{2+}, had little effect on the absorbance at 655 nm because Fe^{3+}/Fe^{2+} has the lowest reduction potential among Co^{3+}/Co^{2+}, Ni_2O/Ni^{2+}, and Mn^{3+}/Mn^{2+}. The absorbance at 655 nm showed a good linear relationship with the Fe^{2+} concentration in the range 0.03–0.83 μmol/L, and the detection limit of Fe^{2+} was 0.03 μmol/L.

Li *et al.* reported **CDs-21** with the pH-dependent photo-oxidation characteristic, which was driven by Ce^{3+} [59]. In the presence of oxygen, **CDs-21** oxidized colorless TMB to blue TMB_{ox} at the natural pH under visible light (Fig. 21). The K_m value of **CDs-21-Ce^{3+}** + EDTA·2Na became lower than that of **CDs-21** with increasing pH, suggesting that **CDs-21-Ce^{3+}** + EDTA·2Na has better affinity for TMB than **CDs-21**. The $^1O_2$ generated from **CDs-21** under light oxidized TMB to TMB_{ox} under acidic conditions. Conversely, under the neutral pH condition, $^1O_2$, which was photo-generated by **CDs-21-Ce^{3+}** + EDTA·2Na under illumination, oxidized Ce^{3+} to Ce^{4+} because the Ce^{3+}/Ce^{4+} potential decreases with increasing pH, and TMB was then further oxidized by Ce^{4+}. Furthermore, the oxidation product Ce^{4+} was the key contributor to oxidation of TMB in a pH neutral environment, and it was stabilized by EDTA·2Na to prevent generation of cerium hydroxide.

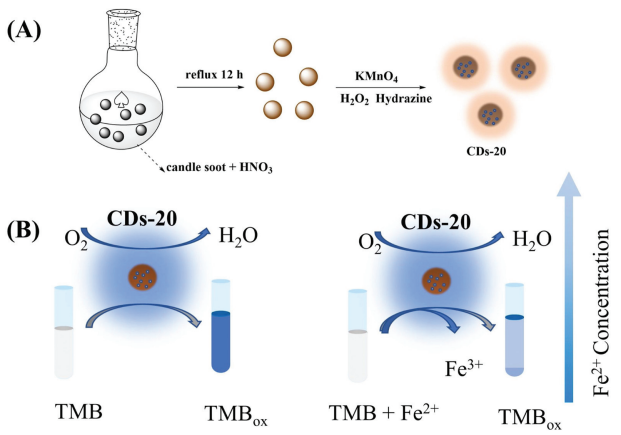

Fig. 20. (A) Synthesis route of **CDs-20**. (B) Schematic illustration of the mechanisms of oxidation of TMB and sensing of Fe^{2+} by **CDs-20**.

2.3. CDs SOD

SOD can transform superoxide radicals to O_2 and H_2O_2 through a disproportionated reaction and then alleviate the oxidative stress caused by cell metabolism. Sun *et al.* reported graphene oxide quantum dots (**CDs-22**) to alleviate ethanol-induced cellular metabolic disturbances [60]. **CDs-22** was purchased from XFNANO Materials (Nanjing, China) and showed good dual catalase- and SOD-like activities (Fig. 22). **CDs-22** increased the activities of intracellular alcohol dehydrogenase and aldehyde dehydrogenase, accelerating conversion of ethanol to acetaldehyde and acetic acid. When the ethanol level in the cells was relatively high, the cell activity, as well as the membrane integrity, was reduced. Upon addition of **CDs-22**, the cell viability and integrity of the membrane were enhanced by nearly 80% compared with the control values, and the excessive autophagy of the endothelial cells caused by ethanol was reduced. Therefore, **CDs-22** was capable of maintaining the integrity of the membrane and reducing the number of damaged endocytes, which were generated to protect the cells from the cell viability decrease caused by ethanol. In addition,

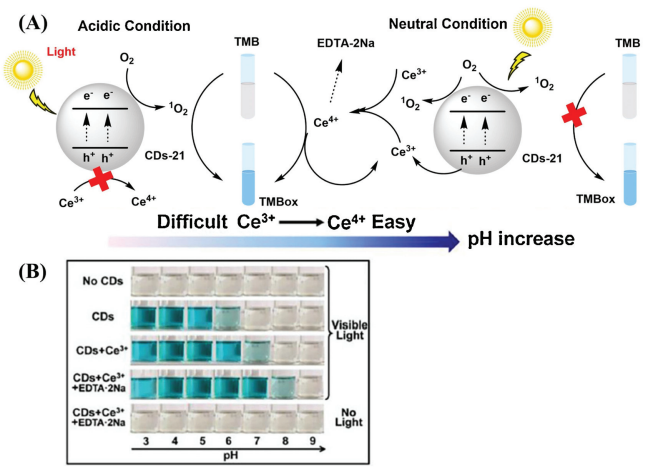

Fig. 21. (A) Mechanism of oxidation of TMB by **CDs-21-Ce^{3+}** + EDTA·2Na in room light. (B) Color changes of TMB under different conditions. Copied with permission [59]. Copyright 2020, Elsevier.

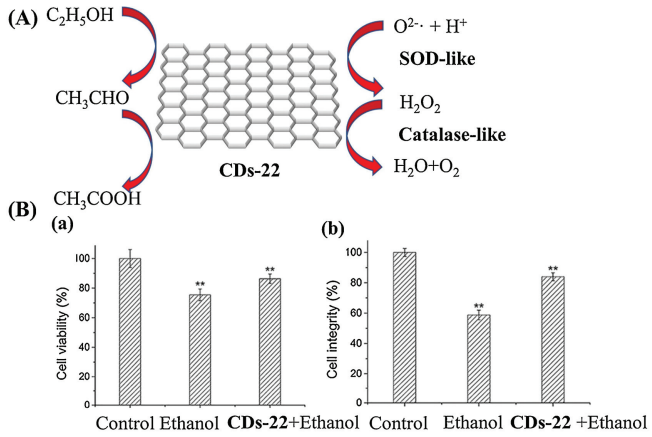

Fig. 22. Proposed mechanism and enzyme-like activities of **CDs-22** for ethanol. (B) (a) Viability and (b) integrity of cells treated with ethanol and **CDs-22** + ethanol, respectively. Reproduced with permission [60]. Copyright 2017, American Chemical Society.

when the cells were treated with ethanol, the concentrations of ROS and malondialdehyde (MDA) increased by about 67% and 117% respectively. Upon addition of **CDs-22**, the ROS and MDA levels decreased and showed negligible differences with the levels of the control group. This suggested that **CDs-22** can reduce the oxidative stress caused by ethanol, and it showed a better alcohol detoxification effect than GSH. Moreover, **CDs-22** can also regenerate ethanol-destroyed cells through repairing ethanol-destroyed proteins. Thus, **CDs-22** can reduce ethanol-induced oxidative stress and promote ethanol and lipid metabolism to increase ethanol detoxification.

Zhao *et al.* reported a nanozyme (**dS-Au-CDs-23**) with dual SOD- and HRP-like activities [61]. **dS-Au-CDs-23** was prepared by loading SOD-like **CDs-23** into the interior surface of dendritic silica spheres (dSs), and HRP-like GSH–Au NPs were linked to the dS surface (Fig. 23). **CDs-23** was synthesized from a mixture of citric acid and EDA by the hydrothermal method. Owing to the wide radial channel in the surface of the dSs, **CDs-23** could be loaded into the inner surface to form **dS-CDs-23**, maintaining the fluorescence signal at 450 nm. The fluorescence intensity of **dS-CDs-23** was enhanced with increasing concentration, and the fluorescence quenching effect of **CDs-23** was eliminated owing to

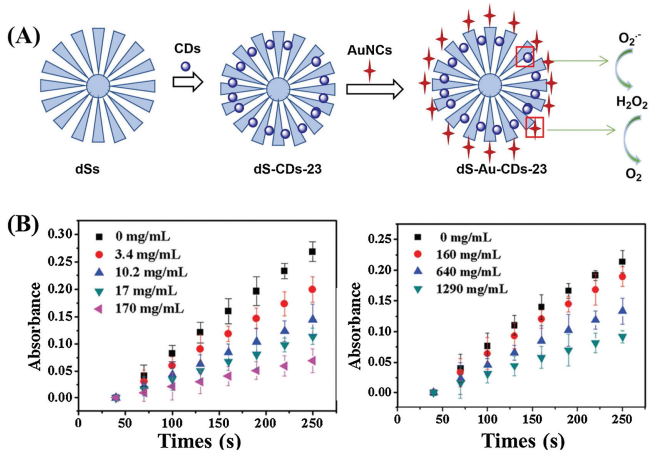

Fig. 23. (A) Synthesis process of **dS-Au-CDs-23** and oxidation mechanism of **dS-Au-CDs-23** with dual SOD- and HRP-like catalytic activities. (B) Changes of the absorption peak at 325 nm with increasing concentration of **CDs-23** and **dS-Au-CDs-23**, respectively. Copied with permission [61]. Copyright 2020, Royal Society of Chemistry.

the distribution in **dS-CDs-23**. Moreover, the fluorescence of **dS-CDs-23** was stronger for higher content of loaded **CDs-23**, indicating that **CDs-23** plays an important role in the fluorescence. **dS-CDs-23** prevented accumulation of the colored intermediates produced by self-oxidization of pyrogallol owing to its SOD-like activity. The typical absorbance at 325 nm can be used to evaluate the activity of **dS-CDs-23**, and it decreased with increasing concentration of CDs, suggesting its high SOD activity. The dSs showed no obvious change in the absorbance at 325 nm with pyrogallol, indicating that the SOD-like activity was indeed from **CDs-23** in **dS-CDs-23**. The GSH-Au NPs also catalyzed oxidation of TMB to TMB_{ox} in the presence of H_2O_2 because of catalyzed generation of $^{\cdot}OH$ from H_2O_2 owing to their HRP-like activity. However, the **dS-Au-CDs-23** loaded GSH-Au NPs also showed excellent HRP-like activity. In conclusion, **dS-Au-CDs-23** exhibits dual SOD- and HRP-like catalytic activities and improves the fluorescence quenching effect of **CDs-23**.

2.4. CDs catalase

Catalase can efficiently convert H_2O_2 to H_2O and O_2. Various nanozymes and nanoparticles with peroxidase- or SOD-like activities possess catalase-mimicking characteristics. Passi *et al.* reported a theranostic nanozyme (**CDs-24**) to simultaneously image and remove ROS [62]. **CDs-24** was self-assembled using a positively charged CD precursor, cationic cerium oxide NPs (CeNPs), and silk fibroin NPs (SFSNPs) loaded with the antioxidant drug sulforaphane. **CDs-24** eliminated the active oxide produced in response to the oxidative stress in the organism (Fig. 24). The CD precursor was prepared from mixed polyethylenimine (PEI) and mulberry leaves, which were heated at 200 °C for 4 h. The CD precursor with green fluorescence strengthened the antioxidant potential of **CDs-24** and promoted imaging. In an acidic environment, the sulforaphane released from the SFSNPs activated the antioxidant response element responsible for antioxidant gene expression in the nucleus. The ROS were removed under the reaction of CeNPs containing Ce^{3+} and Ce^{4+}. When A549 cells were incubated with nonfluorescent DCFH-DA, green fluorescence was observed at 535 nm owing to DCF, which was generated by oxidation of ROS. The cells treated with H_2O_2 showed brighter green fluorescence with DCFH-DA than the above control group. However, when **CDs-24** was added, the green fluorescence from the cells gradually decreased with increasing concentration of **CDs-24**. No fluorescence signal of DCF was detected for only the 100 μg/mL **CDs-24**-treated cells, suggesting that **CDs-24** can efficiently remove ROS in response to oxidative stress.

Dehvari *et al.* developed peroxidase-active CDs (**CDs-25**) to scavenge for free radicals [63]. **CDs-25** was synthesized by the microwave hydrothermal method using citric acid trisodium salt, *N*-acetyl-L-cysteine, manganese acetate, and Na_2S as raw materials (Fig. 25). When TMB was treated with H_2O_2 and Fe^{2+}, the solution changed from colorless to blue, and the characteristic absorption peak of ox-TMB appeared at 652 nm, which was because formation of $^{\cdot}OH$ catalyzed oxidation of TMB. When **CDs-25** was added to the system, the absorbance at 652 nm significantly decreased, which was attributed to removal of $^{\cdot}OH$ by **CDs-25**. In addition, **CDs-25** also exhibited high scavenging capacity for reactive nitrogen species, and 100 μg/mL **CDs-25** showed a 98% scavenging effect for $ONOO^-$. When the surface of **CDs-25** was conjugated with hyaluronic acid (HA), the water solubility of **HA-CDs-25** significantly improved owing to the increase of surface negative functional groups. When B16F1 cells were incubated with 2′,7′-dichlorofluorescin diacetate (DCFH-DA), DCFH-DA was oxidized to green fluorescent dichlorofluorescein (DCF) in the presence of ROS. Upon addition of H_2O_2, the green fluorescence was significantly enhanced. When **HA-CDs-25** was added, the green

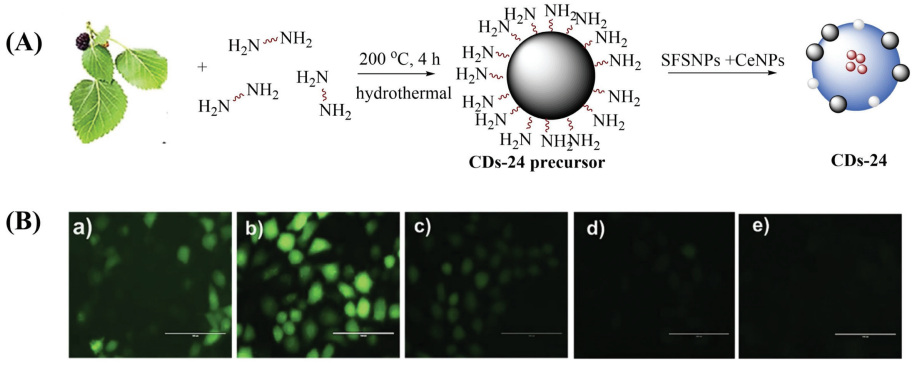

Fig. 24. (A) Synthesis of the CD precursor and **CDs-24**. (B) Images of A549 cells: (a) blank sample, (b) treated with H_2O_2, and (c–e) treated with 20, 60 and 100 μg/mL **CDs-24**, respectively. Reproduced with permission [62]. Copyright 2020, Elsevier.

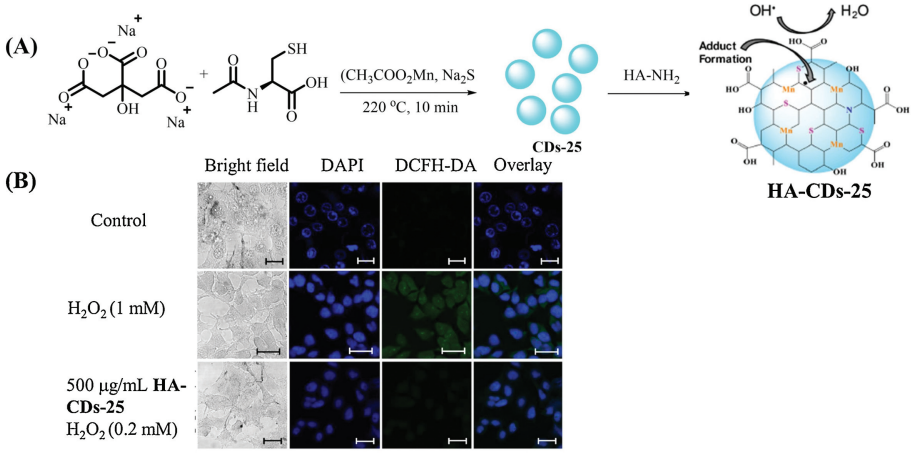

Fig. 25. (A) Synthesis route of **HA-CDs-25** and the corresponding mechanism for reducing ROS. (B) Images of B16F1 cells incubated with DCFH-DA, and then with addition of H_2O_2 (mM: mmol/L) and **HA-CDs-25**. Reproduced with permission [63]. Copyright 2020, Elsevier.

fluorescence signal weakened. When the B16F1 cells were treated with 500 μg/mL **HA-CDs-25** and 0.2 mmol/L H_2O_2, the green fluorescence signal was almost not observed. These results suggested that **HA-CDs-25** can scavenge for ROS in cells.

Wang *et al.* developed a dual-signal indicator (**CDs-26**) with catalase-like activity to detect iodide ions (I^-) in urine by a dual-readout method that can enhance the selectivity and sensitivity, and reduce environmental interference [64]. **CDs-26** was synthesized by hydrothermal reaction at 180 °C for 4 h using ammonium citrate and *o*-aminobenzoic acid (Fig. 26). **CDs-26** emitted bright-blue fluorescence at 450 nm. **CDs-26** could not catalyze oxidation of OPD by H_2O_2 without I^-, but OPD was immediately oxidized by H_2O_2 in the presence of I^-, and it then transformed to OPD_{ox}, accompanied by generation of a yellow color under room light. In addition, the emission intensities at 450 and 565 nm showed a decrease and an increase, respectively, which were attributed to fluorescence resonance energy transfer (FRET). The ratio of the fluorescence at 450 and 565 nm (F_{565}/F_{450}) showed remarkable linearity with the I^- concentration in the range 0.09–50 μmol/L, and the detection limit was 0.06 μmol/L. Although Br^- showed slight interference compared with other ions, the concentration of I^- in urine is much higher than that of Br^- [65,66], suggesting its high selectivity for I^- when used in analysis of real urine samples.

Ren *et al.* reported CDs (**CDs-27**) with catalase-like and antioxidant activities that can efficiently decrease the ROS level and inhibit neurotoxicity [67]. They purchased **CDs-27** from XFNANO (XF042, China). When the 1-methyl-4-phenyl-pyridinium (MPP^+) ion, which can induce oxidative stress, was added to PC12 cells, the α-synuclein level immediately increased (Fig. 27). When **CDs-27** was added, the α-synuclein level decreased, indicating that it inhibited the neurotoxicity *in vitro* through the expression block of α-synuclein. *In vivo*, **CDs-27** could inhibit the neurotoxicity through regulating the metabolism and inhibiting biosynthesis of the important components of the living organism. The corresponding mechanism is shown in Fig. 27. The same phenomenon was observed in zebrafish, and the fluorescence

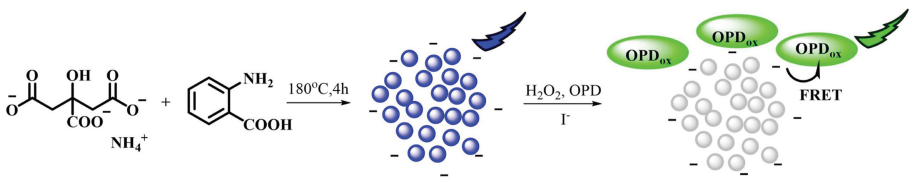

Fig. 26. Synthesis route and proposed mechanism of **CDs-26** for sensing I^- in the presence of OPD and H_2O_2.

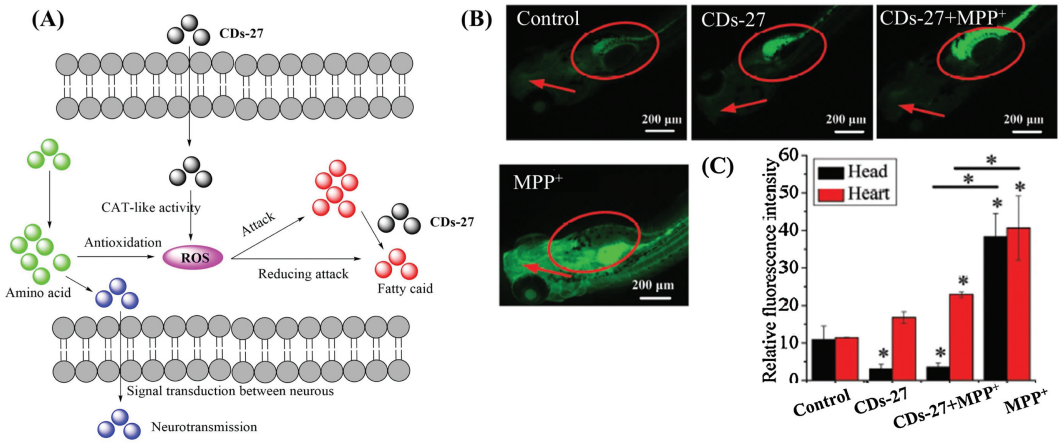

Fig. 27. (A) Schematic of **CDs-27** protecting PC12 cells and larval zebrafish from neurotoxicity and the underlying mechanism. (B) Heads and hearts of zebrafish larvae stained with DCFH-DA. The red arrows indicate the heads and the red ellipses indicate the hearts. (C) Relative fluorescence intensity of (B). Reproduced with permission [67]. Copyright 2020, Wiley Publishing Group.

intensity of the head was much lower than that of heart, suggesting that **CDs-27** was mainly located in the brain to reduce neurotoxicity.

3. Summary and perspective

CDs nanozymes are superior to natural enzymes and other organometallic nanozymes, and they are gradually becoming a research hotspot because of their low cost, stability, environmental favorability, easy of functionalization, outstanding photophysical characteristics, and catalytic activities. Herein, we have reviewed the recent progress in development of CDs nanozymes. Nanozymes have promising prospects in monitoring reactive biological species, theranostics, and tissue imaging. Despite the excellent advances in CDs nanozymes, some critical issues and challenges still need to be resolved through combined efforts.

(1) The structure–activity relationship needs to be determined to realize rational design of CDs nanozymes [68]. Exploring the relationship between the structure of CDs, catalytic sites, and catalytic characteristics should be paid more attention to provide guidance for synthesizing CDs nanozymes with remarkable catalytic performance instead of using the traditional trial-and-error method. We presume that the special groups on the surface of CDs act as the catalytic sites, although further investigation is required. The kinetics and thermodynamics of nanozymes should also be taken into consideration.

(2) The catalytic mechanisms and structure–activity relationship of CDs nanozymes need to be further understood through computational chemistry [69,70]. Because the structure of CDs is extremely complex, more efficient theoretical methods should be used. For example, density functional theory can predict the electronic structure and density.

(3) The number of types of nanozymes should be increased. This could be accomplished by searching for novel catalytic sites or activities in natural enzymes and then synthesizing analogues that are finally incorporated into CDs or by using CDs as the precursor [71,72]. For example, previously reported 1,4-dihydronicotinamide adenine dinucleotide (NADH) oxidase and peroxidase-mimicking nanozymes have mainly been organometallic nanozymes, which are toxic to some extent [73,74]. It would advance the NADH and nanozyme fields if CDs nanozymes with NADH oxidase and peroxidase-like activities were developed owing to their low toxicity and excellent biocompatibility.

(4) Systematically evaluating the efficiency and biocompatibility is extremely important for promoting translational applications of the nanozyme field. For instance, researchers should pay attention to the cellular fate, toxicity, immunogenicity, and therapeutic effect of nanozymes.

In summary, combining the remarkable photophysical properties, water solubility, and biocompatibility of CDs with the remarkable catalytic activities, stability, and low-cost of nanozymes, CDs nanozymes have greatly advanced co-development of the artificial enzyme, CD, and nanotechnology fields. CDs nanozymes have promising prospects in biosensing, photocatalysis, theranostics, biomedicine, and catalytic therapy.

Declaration of competing interest

The authors report no declarations of interest.

Acknowledgments

This work was supported by the National Natural Science Foundation of China (Nos. 21974125, 21708035), the Collaborative Innovation Project of Zhengzhou (Zhengzhou University) (No. 18XTZX12002), and the 111 Project (No. D20003).

References

[1] M. Liang, X. Yan, Acc. Chem. Res. 52 (2019) 2190–2200.
[2] X. Zhang, S. Lin, S. Liu, et al., Coord. Chem. Rev. 429 (2021) 213652.
[3] P. Li, C. Wu, Y. Xu, et al., TrAC Trends Anal. Chem. 131 (2020) 116007.
[4] D. Jiang, D. Ni, Z.T. Rosenkrans, et al., Chem. Soc. Rev. 48 (2019) 3683–3704.
[5] L. Gao, J. Zhuang, L. Nie, et al., Nat. Nanotechnol. 2 (2007) 577–583.
[6] F. Manea, F.B. Houillon, L. Pasquato, P. Scrimin, Angew. Chem. Int. Ed. 43 (2004) 6165–6169.
[7] J. Wu, X. Wang, Q. Wang, et al., Chem. Soc. Rev. 48 (2019) 1004–1076.
[8] H. Qin, Y. Sun, X. Geng, et al., Anal. Chim. Acta. 1106 (2020) 207–215.
[9] X. Geng, Y. Sun, Y. Guo, et al., Anal. Chem. 92 (2020) 7940–7946.
[10] X. Shi, H. Meng, Y. Sun, et al., Small 15 (2019) 1901507.
[11] C. Long, Z. Jiang, J. Shangguan, et al., Chem. Eng. J. 406 (2021) 126848.
[12] S. Lu, L. Sui, J. Liu, et al., Adv. Mater. 29 (2017) 1603443.
[13] H. Song, X. Liu, B. Wang, Z. Tang, S. Lu, Sci. Bull. 64 (2019) 1788–1794.
[14] H. Liu, Y. Sun, Z. Li, et al., Chin. Chem. Lett. 30 (2019) 1647–1651.
[15] Y. Sun, H. Qin, X. Geng, et al., ACS Appl. Mater. Interfaces. 12 (2020) 31738–31744.
[16] C. Xia, S. Zhu, T. Feng, M. Yang, B. Yang, Adv. Sci. 6 (2019) 1901316.
[17] M.L. Liu, B.B. Chen, C.M. Li, C.Z. Huang, Green. Chem. 21 (2019) 449–471.
[18] X. Geng, Y. Sun, Z. Li, et al., Small 15 (2019) 1901517.
[19] H. Liu, Y. Sun, Z. Li, et al., Nanoscale 11 (2019) 8458–8463.
[20] W. Li, Y. Liu, B. Wang, et al., Chin. Chem. Lett. 30 (2019) 2323–2327.
[21] B. Wang, J. Li, Z. Tang, B. Yang, S. Lu, Sci. Bull. 64 (2019) 1285–1292.
[22] J. Fan, P.K. Chu, Small 6 (2010) 2080–2098.
[23] J. Wu, S. Li, H. Wei, Chem. Commun. 54 (2018) 6520–6530.
[24] Y. Zhou, B. Liu, R. Yang, J. Liu, Bioconjugate Chem. 28 (2017) 2903–2909.
[25] J. Wu, S. Li, H. Wei, Nanoscale Horiz. 3 (2018) 367–382.

[26] Y. Li, W. Zhu, J. Li, H. Chu, Colloid. Surf. B. 198 (2021) 111465.
[27] A. Kumar, S. Das, P. Munusamy, et al., Environ. Sci. Nano 1 (2014) 516–532.
[28] B. Unnikrishnan, C.W. Lien, H.W. Chu, C.C. Huang, J. Hazard. Mater. 401 (2021) 123397.
[29] A. Hasan, N.M.Q. Nanakali, A. Salihi, et al., Talanta 215 (2020) 120939.
[30] W. Wang, S. Gunasekaran, TrAC Trends Anal. Chem. 126 (2020) 115841.
[31] M. Shamsipur, A. Safavi, Z. Mohammadpour, Sens. Actuators B: Chem. 199 (2014) 463–469.
[32] S. Yousefinejad, H. Rasti, M. Hajebi, et al., Sens. Actuators B: Chem. 247 (2017) 691–696.
[33] J. Guo, Y. Wang, M. Zhao, Sens. Actuators B: Chem. 297 (2019) 126739.
[34] J. Shi, T. Yin, W. Shen, Colloid. Surfaces. B 178 (2019) 163–169.
[35] L. Zhao, Z. Wu, G. Liu, et al., J. Mater. Chem. B 7 (2019) 7042–7051.
[36] C.Y. Chen, Y.Z. Tan, P.H. Hsieh, et al., ACS Sensors 5 (2020) 1314–1324.
[37] Y. Liu, Q. Zhou, Y. Yuan, Y. Wu, Carbon 115 (2017) 550–560.
[38] F. Wang, C. Zhang, Q. Xue, H. Li, Y. Xian, Biosens. Bioelectron. 95 (2017) 21–26.
[39] N. Shao, H. Wang, X. Gao, R. Yang, W. Chan, Anal. Chem. 82 (2010) 4628–4636.
[40] Q. Li, D. Yang, Y. Yang, Spectrochim. Acta. A. Mol. Biomol. Spectrosc. 244 (2021) 118882.
[41] H.W. Yang, P. Xu, B. Ding, et al., Eur. J. Inorg. Chem. 48 (2019) 5077–5084.
[42] R. Amini, E. Rahimpour, A. Jouyban, Anal. Chim. Acta 1117 (2020) 9–17.
[43] Y. Guo, L. Zhang, S. Zhang, et al., Biosens. Bioelectron. 63 (2015) 61–71.
[44] X. Wang, Y. Lu, K. Hua, D. Yang, Y. Yang, Anal. Bioanal. Chem. 413 (2021) 1373–1382.
[45] A. Ibarbia, L. Sánchez-Abella, L. Lezama, H.J. Grande, V. Ruiz, Appl. Surf. Sci. 527 (2020) 146937.
[46] F. Li, Q. Chang, N. Li, et al., Chem. Eng. J. 394 (2020) 125045.
[47] Y. Li, W. Ma, J. Sun, et al., Carbon. 159 (2020) 149–160.
[48] M. Liang, Y. Wang, K. Ma, et al., Small. 16 (2020) 2002348.
[49] L. Su, Y. Cai, L. Wang, et al., Microchim. Acta. 187 (2020) 132.
[50] D. Yang, Q. Li, S.K. Tammina, Z. Gao, Y. Yang, Sens. Actuators B: Chem. 319 (2020) 128273.
[51] C. Li, Q. Liu, X. Wang, Y. Luo, Z. Jiang, Microchem. J. 159 (2020) 105508.
[52] F. Li, N. Li, C. Xue, et al., Chem. Eng. J. 382 (2020) 122484.
[53] F. Vetr, Z. Moradi-Shoeili, S. Özkar, Appl. Organomet. Chem. 32 (2018) e4465.
[54] P. Ling, Q. Zhang, T. Cao, F. Gao, Angew. Chem. Int. Ed. 57 (2018) 6819–6824.
[55] J. Zhang, X. Lu, D. Tang, et al., ACS Appl. Mater. Interfaces 10 (2018) 40808–40814.
[56] X. Ren, J. Liu, J. Ren, F. Tang, X. Meng, Nanoscale 7 (2015) 19641–19646.
[57] J. Zhang, S. Wu, X. Lu, P. Wu, J. Liu, Nano Lett. 19 (2019) 3214–3220.
[58] F. Honarasa, F. Peyravi, H. Amirian, J. Iran. Chem. Soc. 17 (2020) 507–512.
[59] S. Li, E. Pang, C. Gao, et al., Chem. Eng. J. 397 (2020) 125471.
[60] A. Sun, L. Mu, X. Hu, ACS Appl. Mater. Interfaces. 9 (2017) 12241–12252.
[61] L. Zhao, X. Ren, J. Zhang, et al., New J. Chem. 44 (2020) 1988–1992.
[62] M. Passi, V. Kumar, G. Packirisamy, Mater. Sci. Eng. C 107 (2020) 110255.
[63] K. Dehvari, S.H. Chiu, J.S. Lin, et al., Acta Biomater. 114 (2020) 343–357.
[64] H. Wang, Q. Lu, Y. Liu, et al., Sens. Actuators B: Chem. 250 (2017) 429–435.
[65] R.E. Cuenca, W.J. Pories, J. Bray, Biol. Trace Elem. Res. 16 (1988) 151–154.
[66] Y. Fuse, N. Saito, T. Tsuchiya, Y. Shishiba, M. Irie, Thyroid 17 (2007) 145–155.
[67] C. Ren, X. Hu, Q. Zhou, Adv. Sci. 5 (2018) 1700595.
[68] B. Jiang, D. Duan, L. Gao, et al., Nat. Protoc. 13 (2018) 1506–1520.
[69] H. Wang, K. Wan, X. Shi, Adv. Mater. 31 (2019) 1805368.
[70] M.K. Nazeeruddin, F.D. Angelis, S. Fantacci, et al., J. Am. Chem. Soc. 127 (2005) 16835–16847.
[71] Z. Zhang, Y. Liu, X. Zhang, J. Liu, Nano Lett. 17 (2017) 7926–7931.
[72] E. Golub, H.B. Albada, W.C. Liao, Y. Biniuri, I. Willner, J. Am. Chem. Soc. 138 (2016) 164–172.
[73] L. He, Y. Li, Q. Wu, et al., ACS Appl. Mater. Interfaces 11 (2019) 29158–29166.
[74] Y. Shen, L. Liang, S. Zhang, et al., Nanoscale 10 (2018) 1622–1630.